

Effects of 3D Geometries on Cellular Gradient Sensing and Polarization

Fabian Spill^{1,2}, Vivi Andasari¹, Michael Mak^{1,2},
Roger D. Kamm^{2,*}, Muhammad H. Zaman^{1,*}

May 16, 2022

¹Department of Biomedical Engineering, Boston University, 44 Cummington Street, Boston MA 02215, USA.

²Department of Mechanical Engineering, Massachusetts Institute of Technology, 77 Massachusetts Avenue, Cambridge, MA 02139, USA.

* Co-corresponding authors, rdkamm@mit.edu (RDK), zaman@bu.edu (MHZ)

Abstract

During cell migration, cells become polarized, change their shape, and move in response to various cues, both internal and external. Many existing mathematical models of cell polarization are formulated in one or two spatial dimensions and hence cannot accurately capture the effect of cell shape, as well as the response of the cell to signals from different directions in a three-dimensional environment. To study those effects, we introduce a three-dimensional reaction-diffusion model of a cell. As some key molecules in cell polarization, such as the small GTPases, can exist both membrane bound and soluble in the cytosol, we first look at the role of cell geometry on the membrane binding/unbinding dynamics of such molecules. We derive quite general conditions under which effective existing one or two-dimensional computational models are valid, and find novel renormalizations of parameters in the effective model. We then extend an established one-dimensional cell polarization pathway in our three-dimensional framework. Our simulations indicate that even in some quasi-one-dimensional scenarios, such as polarization of a cell along a linear growth factor gradient, the cell shape can influence the polarization behavior of the cell, with cells of some shape polarizing more efficiently than those of other shapes. We also investigate the role of the previously ignored membrane unbinding rate on polarization. Furthermore, we simulate the response of the cell when the external signal is changing directions, and we find that more symmetric cells can change their polarized state more effectively towards the new stimulus than cells which are elongated along the direction of the original stimulus.

1 Introduction

The ability to migrate is one of the fundamental properties of cells and is observed in both single-celled organisms as well as multicellular organisms in development and tissue maintenance, as well as in disease progression. To migrate in a ordered, directional way, cells need to have the capability to sense and respond to various migratory signals, such as bacteria reacting to nutrients or other attractants or repellents [3, 52], cells being guided to their correct location during embryonic development [4] or immune cells migrating towards locations of injury or infection [30]. Furthermore, cell migration plays a prominent role in diseases such as cancer, where the majority of deaths is caused by metastases. Hence the capability of cancer cells to migrate, invade and metastasize is considered a hallmark of cancer [16, 17].

External stimuli affecting cell migration include biochemical signals [50] or mechanical interactions with the environment [29, 54]. One particularly interesting feature is the capability of many cells to detect spatial variations of concentrations of biochemicals and to migrate towards, or away from the source of such chemical. Often, the gradients of those chemoattractants or repellents have a small slope, so cells need a mechanism to detect and magnify external biochemical stimuli [48]. Such gradient detection then enables the cells to define a polarized state with a well defined front and back. To this purpose, chemical signals need to be translated into the generation of mechanical forces [39], which ultimately enable the cell to migrate into the direction as defined by the polarized state.

In the last few decades, a large number of key molecules has been discovered and studied where they are understood to play an important role in the sensing of chemical stimuli as well as the subsequent polarization, regulation of the actin cytoskeleton and the generation of mechanical forces [46]. Among these molecules are small GTPases [45, 22], PI3K, PTEN, PIPs, [12, 5, 25], Arp2/3 [44, 47] and Cofilin [53, 2].

To understand the complexity of those pathways of interacting molecules, as well as to understand the mechanisms of sensing external gradients and polarization of a cell, a large number of mathematical models of gradient sensing and cell polarization have been developed (see [20, 23] for reviews). Whereas some of these mathematical models try to explain the general principles of signal detection, amplification and polarization [34, 27, 21], others try to explicitly model the dynamics and interactions between some of the most important involved molecules [32, 7, 24, 42, 15, 19]. Many of these models are formulated in terms of reaction-diffusion partial differential equations (PDEs) and make use of ideas such as pattern formation, which have been applied to biology for many years [49, 14, 35, 36]. Alternative modeling approaches to cell polarization include [26], where thermodynamic considerations were used to predict polarization, [51], where the interplay of biochemistry and mechanics on polarization was investigated, or [1], where stochastic cell polarization was considered. The majority of these mathematical models have been formulated, or at least tested, in one or two spatial dimensions. Simulating a model in those lower dimensions greatly decreases the computational costs, and might seem justified if one is

modeling cell migration on two-dimensional substrates or quasi-one-dimensional scenarios such as the detection of a one-dimensional chemical gradient.

However, when the cell has an irregular shape, it is not a priori clear that a lower dimensional mathematical model can be used in such scenarios. Furthermore, in three-dimensional *in vitro* experiments or *in vivo*, stimuli can appear from all directions. An additional complication in three spatial dimensions is the spatial organization of the key molecules behind cell polarization and migration: Some of the regulators of the actin cytoskeleton, like the Arp2/3 complex, are soluble in the cytosol, whereas others such as PIP molecules, are bound to the membrane. Moreover, some molecules such as the small GTPases can be both membrane bound and soluble, and this binding is influenced by the presence of other regulators such as GDI-molecules [8]. Obviously, if the model is formulated in one or two spatial dimensions, there is no formal distinction between membrane and cytosol. Some mathematical models such [31] have studied the influence of cell geometries on cell polarization and migration in two dimensions, the role of cell shape on signaling [37], the mechanical effects of shape on cell migration [18], the effect of cell shape on stress fiber polarization [55], or the effect of signaling on cell shape [6, 9], see also the review [38]. A mathematical model focusing specifically on the effect of shape on cell polarization, taking into account a whole polarization pathway, has, to our knowledge, not been investigated.

For the above-mentioned reasons, we are studying the effect of the cell shape on gradient sensing and cell polarization in a three-dimensional mathematical reaction-diffusion model of key molecules involved in polarization. We first study a toy-model of a sample molecule, which can bind and unbind from the membrane in section 2. Such molecules could represent, for instance, the small GTPases. We then study the reduction of this model to one and two-dimensional geometries. We obtain conditions when effective one or two-dimensional models can be used, and when the membrane binding/unbinding kinetics can be ignored. These results are general and valid for any molecule involved in binding and unbinding from the membrane, and hence also for polarizing cells of various kinds. Then, in section 3, we investigate a three-dimensional version of the one-dimensional model [19], which was originally developed to study the polarization of migrating HeLa cells. It is based on the dynamics of the small GTPases Rac, Rho and CDC42, as well as PIP, PIP2 and PIP3. As those molecules also play a key role in many other migrating cells, both of mesenchymal and amoeboidal migration type[11, 41], we expect that our results could, qualitatively, also be valid for many other cell types. We focus on the model [19] as, unlike other one-dimensional models, the geometric effect of changing the length of the cell was thoroughly investigated. We find similar, but quantitatively different results regarding the effect of the length in our model. Furthermore, we identify situations where the cell shape influences the capability and time scales of the cell to polarize as well as to adapt when the stimulus changes directions. In particular, we find that cells elongated along an initial polarization direction are less able to repolarize towards a new stimulus perpendicular to the initial stimulus than more spherical cells. Indeed, this is compatible with the fact that more elongated cells migrate more persistently, as reviewed in [43]. We also find that varying the membrane binding and unbinding rate can change the cell

polarization behavior. The results in this paper predict that cell shape is an important factor influencing the ability of a cell to sense external signals, polarize and ultimately migrate.

2 Model for Membrane-Cytosol Binding

As we described in the introduction, a fundamental difference of three-dimensional cell polarization models to their lower dimensional analogues is that we have to couple membrane-bound molecules to those diffusing in the cytosol. Reactions which only take place in the cytosol or on the membrane are straightforwardly implemented, so in this section, we explore a toy model which focuses on the binding-unbinding reactions to and from the membrane. We consider a single molecule that can exist in two states: freely diffusing in the cytosol or freely diffusing on the membrane. When a molecule in the cytosol is close to a membrane, it can bind to the membrane, or when it is bound to the membrane, it can unbind. Typical examples for such a molecule are the small GTPases. We ignore all other reactions of the GTPases with other molecules, as well as activation and deactivation, *i.e.* swapping between GDP and GTP bound states, in this section and explore some of those reactions in later sections. The results in this section are quite general and are expected to be valid for most cell types and migratory modes, as most of those, in some form or another, involve molecules such as the GTPases which exist in a membrane-bound form, or sequestered into the cytosol [41].

2.1 3D Membrane-Cytosol Interaction Model

We denote by c the density of molecules which are freely diffusing in the cytosol, measured in moles per volume, and by m the density of membrane-bound molecules, measured in moles per area. L_I is the interaction length such that when a molecule in the cytosol is within a distance less or equal to L_I of the membrane, there is a probability of binding this molecule to the membrane. The associated binding rate is denoted by k_{on} . Likewise, unbinding is denoted k_{off} , and the diffusion coefficients for diffusion in the cytosol or on the membrane, respectively, are denoted D_C and D_M . Then, m and c evolve according to the following PDEs:

$$\begin{aligned} \frac{\partial m(\bar{r}_m, t)}{\partial t} &= D_M \nabla_2^2 m(\bar{r}_m, t) + k_{on} L_I c(\bar{r}_m, t) - k_{off} m(\bar{r}_m, t) \\ \frac{\partial c(\bar{r}_c, t)}{\partial t} &= D_C \nabla_3^2 c(\bar{r}_c, t) \\ -D_C e_n \nabla c(\bar{r}_m, t) &= k_{on} L_I c(\bar{r}_m, t) - k_{off} m(\bar{r}_m, t). \end{aligned} \quad (1)$$

The boundary condition for c ensures conservation of the number of molecules under binding and unbinding, and e_n is the unit normal vector at the membrane. \bar{r}_m and \bar{r}_c denote points on the membrane or in the cytosol, respectively.

2.2 One-Dimensional Reduction

We now consider the reduction of equation (1) to a cylindrical cell where the height of the cell is L and the radius is R , where we assume cylindrical symmetry and no strong dependence in the radial direction of the cylinder. Then, (21) reduces to

$$\begin{aligned}\frac{\partial \tilde{m}(z, t)}{\partial t} &= D_M \partial_z^2 \tilde{m}(z, t) + 2k_{on} \frac{L_I}{R} \tilde{c}(z, t) - k_{off} \tilde{m}(z, t), \\ \frac{\partial \tilde{c}(z, t)}{\partial t} &= D_C \partial_z^2 \tilde{c}(z, t) + \left(k_{off} \tilde{m}(z, t) - 2k_{on} \frac{L_I}{R} \tilde{c}(z, t) \right).\end{aligned}\quad (2)$$

Note that while these equations are perfectly one-dimensional PDEs, with the spatial domain defined by the length of the cylinder, so $0 \leq z \leq L$, the cylinder radius is still felt in the sense that the membrane-binding rate k_{on} is effectively renormalized by the inverse of the cylinder radius R . At fixed cylinder volume, when we increase the length of the cylinder, R will decrease, so the effective membrane binding rate $2k_{on} \frac{L_I}{R}$ will increase. This makes intuitive sense as for a longer and thinner cylinder, proportionally more molecules in the cytosol are close to the membrane. Indeed, the thin layer of width L_I around the membrane, which is the region of the cytosol accessible to membrane-binding of the molecules, becomes larger for smaller R , under fixed cylinder volume. We discuss the derivation of equation (2) as well as its generalization to other quasi-one dimensional geometries in the section A.3.

2.2.1 Binding-Unbinding Equilibrium

We now consider the equilibrium condition between the binding and unbinding to and from the membrane in a cylindrical cell as implied from equation (2), $\frac{2L_I}{R} k_{on} \tilde{c}(z, t) = k_{off} \tilde{m}(z, t)$. The rates of binding and unbinding are set by k_{off} and $\frac{2k_{on}L_I}{R}$, respectively. As of now, we do not consider other reactions, so we only compare those rates to the timescales of membrane and cytosol diffusion. In the direction of the cylinder axis these are given by the rates $\frac{D_M}{L^2}$, $\frac{D_C}{L^2}$, respectively. As $D_C \gg D_M$, it suffices to have $k_{off} \gg \frac{D_C}{L^2}$, $\frac{2k_{on}L_I}{R} \gg \frac{D_C}{L^2}$ for the assumption that binding and unbinding is fast, relative to diffusion in the direction of the cylinder axis. Note that the derivation of the one-dimensional reduction made use of a condition given by equations (18) in the appendix which imply that the diffusion rate into the radial direction $\frac{D_C}{R^2}$ is necessarily faster than the binding and unbinding rates. This apparent contradiction to considering the binding-unbinding quasi steady state is resolved by considering approximate cylindrical symmetry and homogeneity in the radial direction, as we have done to justify the use of the one-dimensional model. In this case, provided that the total constraint

$$\begin{aligned}\frac{D_C}{R^2} &\gg k_{off} \gg \frac{D_C}{L^2}, \\ \frac{D_C}{R^2} &\gg \frac{2k_{on}L_I}{R} \gg \frac{D_C}{L^2}.\end{aligned}\quad (3)$$

is valid, we can consider simultaneously the reduced one-dimensional model and the steady-state assumption between bound and unbound molecules. If we have

exact radial homogeneity, there is no radial diffusion and we can also ignore the radial diffusion rate $\frac{D_C}{R^2}$. If f denotes the fraction of membrane-bound to total concentration, then f is given by

$$f = \frac{k_{on}}{k_{on} + k_{off} \frac{R}{2L_I}} = \frac{k_{on}}{k_{on} + k_{off} \sqrt{\frac{V}{4\pi L_I^2 L}}}. \quad (4)$$

Note that this formula is similar to one given in [19], but we have a square root dependence on the ratio of volume to length. This discrepancy seems to be caused by the fact that in [19] the membrane concentration was not measured in the same units as the cytosolic concentrations in the reduced model¹. For a general geometry, equation (4) generalizes to

$$f = \frac{k_{on}}{k_{on} + k_{off} \frac{V}{L_I S}}, \quad (5)$$

where S is the surface area and V the volume of the geometry under consideration. Then, we can introduce an effective diffusion coefficient $D_{MC} = fD_M + (1-f)D_C$, as in [7, 19], so that the total concentration $c_{tot}(z, t) = \tilde{c}(z, t) + \tilde{m}(z, t)$ simply evolves by the standard one-dimensional diffusion equation

$$\frac{\partial c_{tot}(z, t)}{\partial t} = D_{MC} \frac{\partial^2 c_{tot}(z, t)}{\partial z^2}. \quad (6)$$

We have thus reduced the original system of two coupled PDEs in three spatial dimensions to a single PDE in one spatial dimension. Note that other potential reactions in the system would need to be modified by f accordingly.

2.3 Two-Dimensional Reduction

Let us consider a flat cell, which, for simplicity, we take to be a disk of radius R and height h . Hence, it is natural to choose cylindrical coordinates, assuming that $R \gg h$, so we ignore the h -dependence. Then, equations (1) reduce to

$$\begin{aligned} \frac{\partial \tilde{m}(r, \phi, t)}{\partial t} &= D_M \nabla_2^2 \tilde{m}(r, \phi, t) + 2k_{on} \frac{L_I}{h} \tilde{c}(r, \phi, t) - k_{off} \tilde{m}(r, \phi, t), \\ \frac{\partial \tilde{c}(r, \phi, t)}{\partial t} &= D_C \nabla_2^2 \tilde{c}(r, \phi, t) - 2k_{on} \frac{L_I}{h} \tilde{c}(r, \phi, t) + k_{off} \tilde{m}(r, \phi, t). \end{aligned} \quad (7)$$

Introducing $\tilde{k}_{on} = 2k_{on} \frac{L_I}{h}$ we formally recover the two-dimensional model used in [32]. Similarly to the one-dimensional case, we find that the parameters of the reduced geometry, in this case, the cylinder height h , renormalize the effective membrane-binding coefficient. As before, we consider the steady-state solution where f denotes the fraction of membrane-bound molecules. We get

$$f = \frac{k_{on}}{k_{on} + k_{off} \frac{h}{2L_I}}. \quad (8)$$

¹We thank Bill Holmes for useful discussions about this point

3 A Three-Dimensional Model of Cell Polarization

We now focus on a three-dimensional cell polarization model incorporating the three GTPases Rac, Rho and Cdc42, as well as the three Phosphoinositides PIP1, PIP2 and PIP3 as dynamic quantities. We use the interactions as in model 4 of [19], where a one-dimensional model for HeLa cell migration was investigated. The full model is given in the appendix, section B. We will then consider quasi-one-dimensional cells to show that we can reproduce the results of [19]. Furthermore, we will go on to study cells with other geometries to exploit the gained generality of this model compared to previous models, and show scenarios not possible to explore in one-dimensional models. All simulations in this section were performed in COMSOL Multiphysics 5.0/5.1 (COMSOL, Inc, Burlington, MA) using the General PDE model framework. We remark that the default solver occasionally produced too large time steps, requiring us to manually limit the maximal time step depending on the model parameters. All 3D plots produced in this section show membrane concentrations measured in $\frac{\text{mol}}{\text{m}^2}$, with the numbers at the top and bottom of the color charts denoting the maximal and minimal concentrations, respectively.

3.1 Polarization of a Quasi-One-Dimensional Cell

To compare to the one-dimensional model [19], we are now investigating a scenario of emerging polarization where we start with initially homogeneous concentrations of all molecules, which are then perturbed by a large spike in active Rac in one end of the long cell in a symmetric way depending only on the direction of the longest extent of the cell. First of all, we checked our code on a cell shaped as a cuboid with side lengths $L, w, d = 20, 8, 5\mu\text{m}$, as this best resembles a quasi-one-dimensional geometry. Figure 1 shows a typical time evolution of a GTPase concentration, here CDC42, after the initial Rac stimulus is applied at time $t = 0$ at the bottom of the cell. We see that at time $t = 20\text{s}$ it looks as if the cell could polarize, but the strength of polarization fades away and is completely absent at time $t = 200\text{s}$. As we are interested in studying the effect of geometry in this paper, we are varying the length of the cell, fixing the cell volume to $V = 800\mu\text{m}^3$.

Figure 2 shows this cell with different lengths, $L = 40, 80\mu\text{m}$. In each case we perturbed active Rac at the bottom of the cell and show the active Cdc42 concentrations after $t = 200\text{s}$. We see that in both cases a stable polarization pattern is established. This is in contrast to the case of the shorter cell with $L = 20\mu\text{m}$, which, as shown in Figure 1, has no signs of polarization after $t = 200\text{s}$. Figure 7 in the appendix shows results from the same simulations but focuses on the time series of active CDC42 at the front and back of the cell. These results are compatible with the observation in [19] that length can change the bifurcation behavior and increase the polarization sensitivity. However, the numeric are different as we take the finiteness of the membrane binding and unbinding into account, and the fraction of membrane-bound GTPases which we derived in section 2.2 was slightly different from the one used in [19].

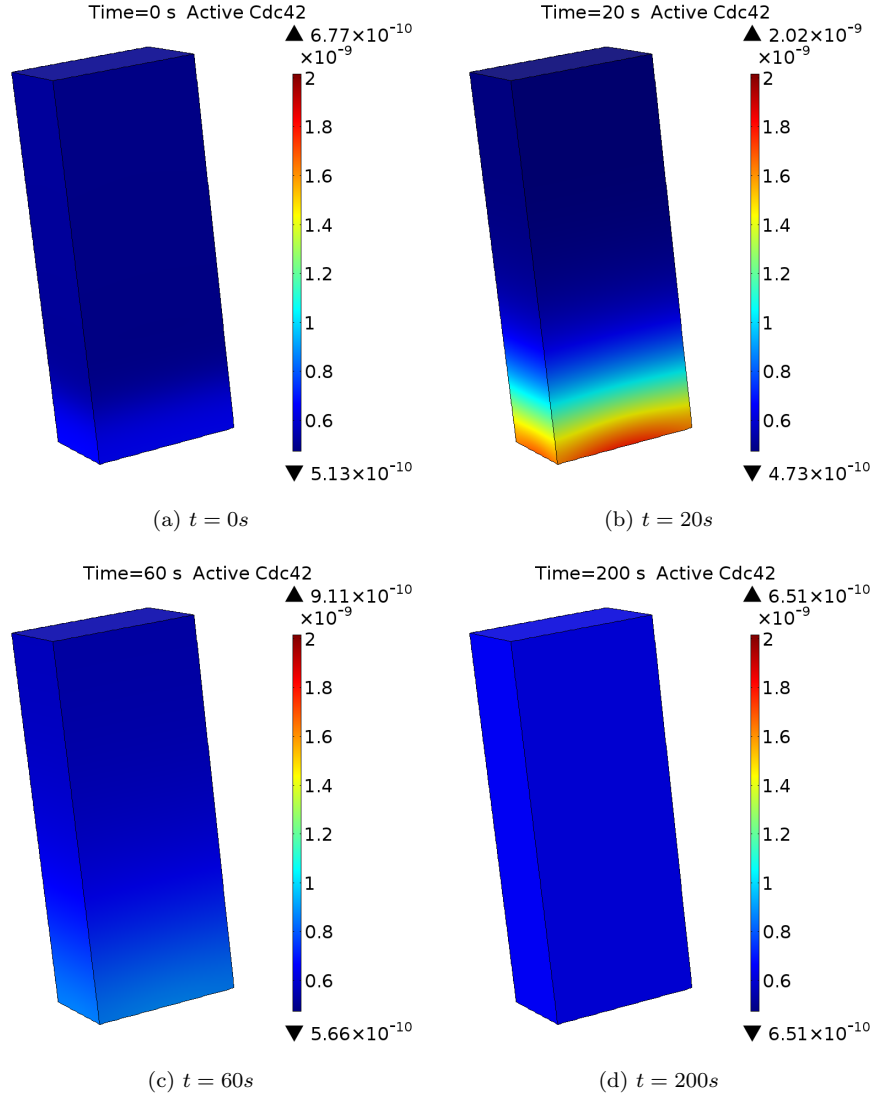


Figure 1: We show the concentration of active Cdc42 on the membrane for a rectangular cell with lengths $L, w, d = 20, 8, 5 \mu m$. Active Rac is perturbed at the bottom of the cell, leading to a brief polarized state which then fades away with progressing time.

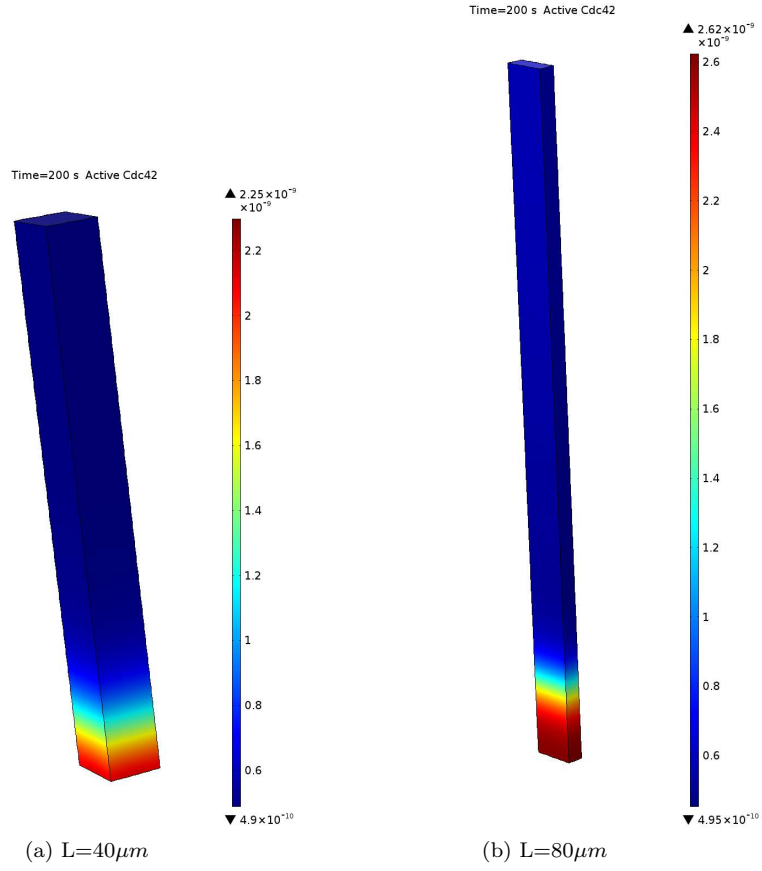


Figure 2: The same cell and setup as in Figure 1, but elongated to $L = 40$ and $80\mu m$. We see that, contrary to the cell with $L = 20\mu m$ shown in Figure 1(d), after 200s a stable polarized state is maintained.

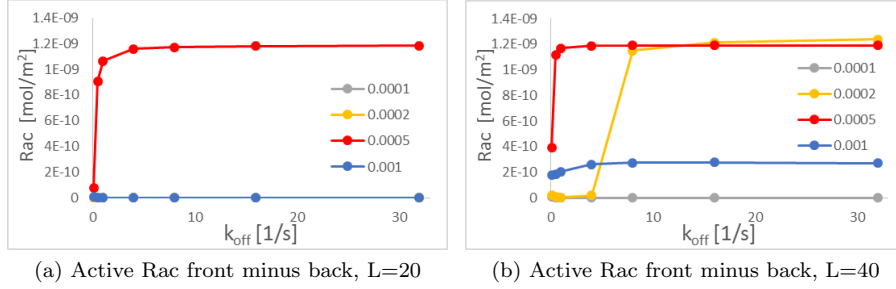


Figure 3: As a measure of polarization strength, we compare the difference in concentrations of active Rac at the front and the back of the cell in dependence on k_{off} for different values of the Rac activation rate $I_{R1} = 0.0001, 0.0002, 0.0005, 0.001 \frac{\text{mol}}{\text{m}^3\text{s}}$ and two length, $L = 20\mu\text{m}$, (a), and $L = 40\mu\text{m}$, (b), in all cases 200 seconds after an initial stimulus of active Rac is applied at the front of the cell. In (a), only the cell with $I_{R1} = 0.0005$ shown in red is polarized, and all three other values lead to completely unpolarized states.

3.2 Parameter Investigation

We now investigate the dependence of our model on some key parameters. The one-dimensional model [19] already identified the Rac activation rate I_{R1} as playing a key role, with results from local perturbation analysis indicating an intermediate regime of I_{R1} capable of maintaining multiple steady states, but both low and high values of I_{R1} imply that only one steady state is present. Furthermore, it was found in [19] that the length of the cell can effect the I_{R1} -dependence of the steady states. Since we obtained a different quantitative relation for the length dependence of the fraction of active GTPases than in [19], we check numerically if we get a similar length dependence. As discussed before, an important new parameter is the membrane unbinding rate k_{off} and its associated binding rate k_{on} , which we fix via relation (5) under fixing f . Its role in cell polarization was, to our knowledge, not investigated in detail in previous work. Figure 3 shows the difference of active Rac at the front and back of a rectangular cell as a function of k_{off} 200s after an initial stimulus of Rac at the front. Figure 3(a) shows a cell of length $L = 20\mu\text{m}$, whereas Figure 3(b) shows a cell of $L = 40\mu\text{m}$. In each case, we show plots for 4 different Rac activation rates I_{R1} . First, we confirm qualitatively the observation of [19] that intermediate ranges of I_{R1} can lead to a polarized states, or are stronger polarized. Furthermore, the shorter cell does not polarize as easily as the longer cell, as in Figure 3(a) only the cell with $I_{R1} = 0.0005$ is polarized. We also see that k_{off} is positively associated with polarization strength, and the cells with very small values of $k_{off} = 0.1\text{s}^{-1}$ do not or only weakly polarize. Note that (3) implies $k_{off} \gg \frac{D_G}{L^2} = \frac{1}{4}\text{s}^{-1}, \frac{1}{16}\text{s}^{-1}$ for $L = 20, 40\mu\text{m}$, respectively, so in neither case is the model of [19] necessarily expected to be accurate. We also note that for most, but not all parameters checked, the polarization strength saturates at k_{off} values of the order of magnitude of 1s^{-1} .

3.3 Influence of Geometry on Polarization

We now investigate how cell shape influences the ability of the cell to polarize, loose polarization or repolarize when the direction of a signal changes in time. Here we include effects which cannot be investigated with a one-dimensional model.

3.3.1 Influence of Geometry on Initial Polarization

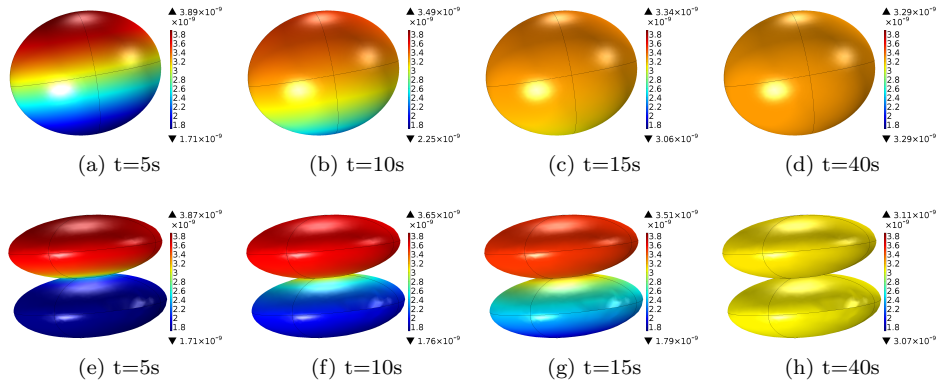


Figure 4: The same cell (with the same volume, same length and similar surface area) once spherical (top row) and once as two connected ellipsoids, so very thin in the middle (bottom row), polarized by an initial perturbation of active Rac at the top. Shown is the distribution of active Rac for those two cell shapes at different times for a scenario where the stimulus is not sufficient to permanently keep the cell in a polarized state. However, we can see that the thinned out cell stays in a polarized state for considerably longer than the spherical cell.

In Figure 4 we see active Rac on the membrane of the same cell polarizing under an initial stimulation of Rac with a step function with two-different geometries. This step function is adjusted in such way that the total initial amount of active Rac is the same in both scenarios. Figures 4(a)-(d) show the polarization when the cell is spherically shaped, whereas Figures 4(e)-(h) show the the same cell which is thinned out in the middle, but with the same volume. We see that the spherical cell loses this initial polarization rather quickly, after about 15s, whereas the thinned out cell is still well polarized at this time. Ultimately, in this scenario, the cell loses the polarization after about 40s with both geometries.

3.3.2 Response of Cell to a Change in Stimulus Direction

Figure 5 shows active Rac for a cell of a volume of $V = 800\mu\text{m}^3$ for three different Ellipsoidal configurations: With a main axis of $11.5\mu\text{m}$ (spherical, (a)-(d)), $20\mu\text{m}$ ((e)-(h)) and $40\mu\text{m}$ ((i)-(l)). Initially a stable polarized state is obtained in all three configurations, which is shown at $t = 100\text{s}$ just before the

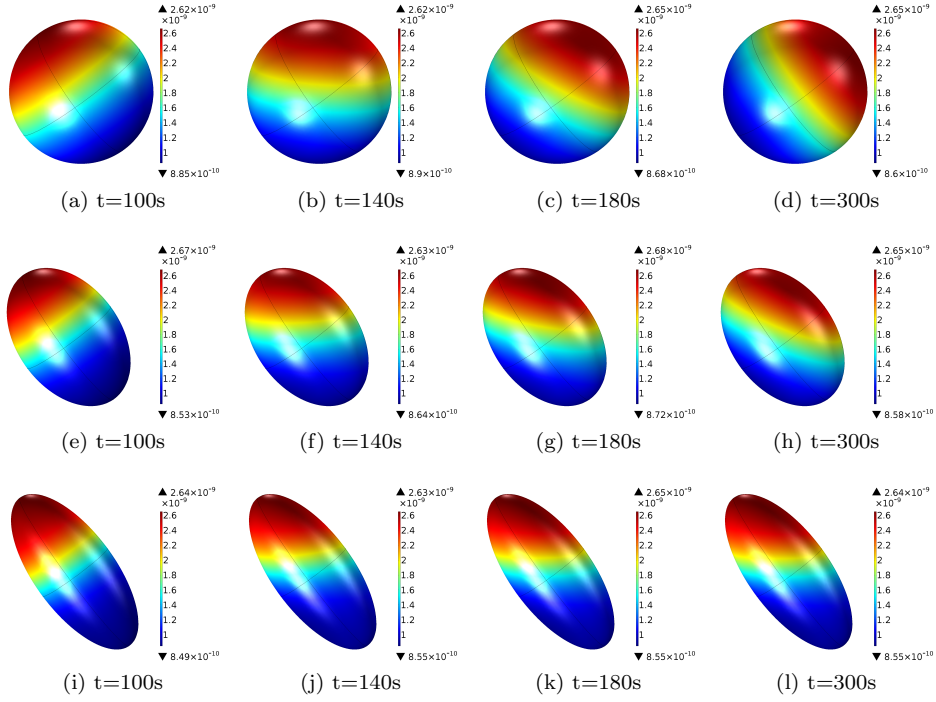


Figure 5: Active Rac on the membrane is shown for different times for the same cell with different shapes, where the Rac activation rate is directional in such a way that in the first 100s, the stimulus is linearly increasing with the axis defined from the left upper to right lower corner, whereas for larger times, it increases along the axis defined along the left lower to the right upper corner. We consider an ellipsoidal cell with a fixed volume $V = 800\mu m^3$ and a main axis of $11.5\mu m$ (spherical, (a)-(d)), $20\mu m$ ((e)-(h)) and $40\mu m$ ((i)-(l)). Comparing the different shapes, we see that only the spherical cell can completely polarize into the new stimulus direction, whereas the cells with the ellipsoidal shapes will form a stable pattern which points into a direction in between the original and final stimulus direction.

activation gradient direction is changed. The spherical cell always maintains a main direction, but the direction of polarization rotates towards the new stimulus direction. At $t = 180s$ the cell is mainly polarized into the new stimulus direction (c), and at $t = 300s$ it is completely repolarized. Interestingly, the ellipsoidal configurations never reach a polarized states aligned with the new stimulus. Instead, the new polarization direction is somewhere in between the original and final stimulus direction, and the larger the ratio of the main axes is, the closer the new polarization direction will remain to the original polarization direction. This would suggest that a more symmetric, spherical cell is able to repolarize faster and more efficiently than a long, thin cell. Note that this is compatible with the finding that more elongated cells migrate more directional and persistent, as reviewed for fibroblasts in [43].

4 Discussion

Motivated by the fact that cells, both in *in vitro* and *in vivo* environments, present with greatly varying shapes, we have investigated how cell shape influences gradient detection and cell polarization in this paper. For molecules such as small GTPases, which can exist both in a membrane bound form as well as sequestered in the cytosol, the ratio of cell volume to surface area can influence important properties such as the fraction of membrane-bound molecules, as seen in equation (5). Furthermore, we found that even in the dimensionally reduced models the higher dimensions implicitly appeared in the reduced equation by renormalizing the membrane binding rate (equation (2)). We also found conditions on the parameters which, when satisfied, justify the use of the lower dimensional models (equation (18)). These conditions are quite general and should be useful both to check the validity of older model as well as for the development of new models which involve interactions of molecules between membrane and cytosol.

In our model, we have only considered constant membrane binding and unbinding rates for a molecule to and from the membrane, and investigated how this rate affects the polarization behavior of a cell (Figure 3). In real cells, the binding and unbinding from the membrane as well as activation and deactivation of small GTPases is influenced by the presence of a large number of different GDI, GEF and GAP molecules, respectively [13]. It would be interesting to include the effect of those regulating molecules in our model. However, at present, there is a lack of good quantitative data regarding those molecules, so we postpone such investigations for future research. What Figure 3 confirmed is that the binding/unbinding rate can influence the ability of a cell to polarize, and as GDI molecules are expected to modify those rates the model predicts that the presence or absence of these molecules will also affect the polarization behavior.

We then extended an established cell polarization pathway [19], which was previously investigated in a one-dimensional model of HeLa cells, to our three-dimensional model. The purpose of choosing [19] for comparison was that in this model, the effect of changing the cell length was implicitly taken into account via a modification of the fraction of membrane-bound GTPases, whereas

most other one-dimensional models did not consider any geometric effects at all. Hence, a first test of our model was to reproduce the results of [19]. We observed qualitatively the same dependence of cell polarization on the cell length as well as the Rac activation rate as [19]; however, quantitatively we obtained different results, as our derivation of the fraction of membrane-bound GTPases yielded a different dependence (equation (5)) on the length than the one found in [19]. Furthermore, as mentioned above, we are, to our knowledge, the first to explicitly consider the binding/unbinding dynamics of the GTPases to the membrane, and showed the influence of those parameters on the polarization behavior of the cell in Figure 3.

Having reproduced the essential behavior in quasi-one-dimensional cells of existing models, we went on to explore scenarios which the existing lower dimensional models could not capture. First, we compared the polarization behavior of two cells with the same volume and length, but one spherical and one thinned out in the middle. Such thinning can happen in real cell cultures, e.g. in the HeLa cells used in [28]. The results shown in Figure 4 confirmed that these cells have a different polarization behavior, with the spherical cell loosing its polarized state considerable faster than the cell which is thinned out in the middle. This result is important whenever one is trying to compare theoretical results obtained from simplified lower dimensional models to experiments, indicating that one has to take cell shape into account. We expect that the behavior of pathways other than those describing polarization would also be affected by cell shape in a similar manner, and that the results are valid for cell types other than HeLa cells, if the principle mechanism of polarization is mediated by similar reaction-diffusion models as the ones used here.

As long as the polarization stimulus is coming from only one direction, and provided the parameter constraints (18) are satisfied, one-dimensional models could still be derived which take into account the varying cross section of the cell along the stimulus direction by effectively modifying the diffusion coefficient, as we show in appendix A.3.1. However, stimuli purely in one-direction are idealistic and *in vivo* different stimuli can appear from all directions and change in time. In the study of such effects we have to use three-dimensional models such as ours. In Figure 5 we simulated a stimulus which was changing directions over time. We found that cell shape is an important factor which predicts how fast and strong a cell can adapt to the new direction of stimulus. Indeed, the spherical cell was able to change the internal polarization direction smoothly towards the new stimulus direction, whereas cells which are elongated along the previous direction of stimulus preferentially stayed polarized in a direction close to the original stimulus. This prediction is compatible with the observation that elongated cells often migrate more directional and persistent, see [43]. However, varying the stimulus direction was not tested in those setting. An explicit test of the model could be, for instance, in a microfluidics platform where one can change the direction of an external growth factor gradient over time, and measures the response of some tagged internal molecule associated with polarization in dependence of the cell shape.

In summary, the results in this paper predict the importance of cell shape on polarization of cells, indicate in which cases the use of lower dimensional models

is justified, and when a full three-dimensional model such as ours needs to be used to model and predict experimental results.

5 Author Contributions

FS designed research, performed research, analyzed data and wrote the paper, VA and MM contributed analytic tools, RDK and MHZ designed research and wrote the paper.

6 Acknowledgment

We acknowledge the support of the NCI grant number 5U01CA177799. We are also grateful to Leah Edelstein-Keshet, Bill Holmes, Philip Maini and Frits Veerman for useful discussions.

References

- [1] Steven J Altschuler, Sigurd B Angenent, Yanqin Wang, and Lani F Wu. On the spontaneous emergence of cell polarity. *Nature*, 454(7206):886–889, 2008.
- [2] Silvia Arber, Freda A Barbayannis, Hartwig Hanser, Corinna Schneider, Clement A Stanyon, Ora Bernard, and Pico Caroni. Regulation of actin dynamics through phosphorylation of cofilin by lim-kinase. *Nature*, 393(6687):805–809, 1998.
- [3] Howard C Berg and Edward M Purcell. Physics of chemoreception. *Biophysical journal*, 20(2):193, 1977.
- [4] Bruce M Carlson. *Human embryology and developmental biology*. Elsevier Health Sciences, 2013.
- [5] Megan Cully, Han You, Arnold J Levine, and Tak W Mak. Beyond pten mutations: the pi3k pathway as an integrator of multiple inputs during tumorigenesis. *Nature Reviews Cancer*, 6(3):184–192, 2006.
- [6] Maitreyi Das, Tyler Drake, David J Wiley, Peter Buchwald, Dimitrios Vavylonis, and Fulvia Verde. Oscillatory dynamics of cdc42 gtpase in the control of polarized growth. *Science*, 337(6091):239–243, 2012.
- [7] Adriana T Dawes and Leah Edelstein-Keshet. Phosphoinositides and rho proteins spatially regulate actin polymerization to initiate and maintain directed movement in a one-dimensional model of a motile cell. *Biophysical journal*, 92(3):744–768, 2007.
- [8] Athanassios Dovas and John Couchman. Rhogdi: multiple functions in the regulation of rho family gtpase activities. *Biochem. J*, 390:1–9, 2005.

- [9] Tyler Drake and Dimitrios Vavylonis. Model of fission yeast cell shape driven by membrane-bound growth factors and the cytoskeleton. *PLoS Comput Biol*, 9(10):e1003, 2013.
- [10] Harold P Erickson. Size and shape of protein molecules at the nanometer level determined by sedimentation, gel filtration, and electron microscopy. *Biol Proced Online*, 11(1):32–51, 2009.
- [11] Peter Friedl. Prespecification and plasticity: shifting mechanisms of cell migration. *Current opinion in cell biology*, 16(1):14–23, 2004.
- [12] Satoru Funamoto, Ruedi Meili, Susan Lee, Lisa Parry, and Richard A Firtel. Spatial and temporal regulation of 3-phosphoinositides by pi 3-kinase and pten mediates chemotaxis. *Cell*, 109(5):611–623, 2002.
- [13] Rafael Garcia-Mata, Etienne Boulter, and Keith Burridge. The ‘invisible hand’: regulation of rho gtpases by rhogdis. *Nature reviews Molecular cell biology*, 12(8):493–504, 2011.
- [14] Alfred Gierer and Hans Meinhardt. A theory of biological pattern formation. *Kybernetik*, 12(1):30–39, 1972.
- [15] Andrew B Goryachev and Alexandra V Pokhilko. Dynamics of cdc42 network embodies a turing-type mechanism of yeast cell polarity. *FEBS letters*, 582(10):1437–1443, 2008.
- [16] Douglas Hanahan and Robert A Weinberg. The hallmarks of cancer. *Cell*, 100(1):57–70, 2000.
- [17] Douglas Hanahan and Robert A Weinberg. Hallmarks of cancer: the next generation. *Cell*, 144(5):646–674, 2011.
- [18] Marc Herant and Micah Dembo. Form and function in cell motility: from fibroblasts to keratocytes. *Biophysical journal*, 98(8):1408–1417, 2010.
- [19] William R Holmes, Benjamin Lin, Andre Levchenko, and Leah Edelstein-Keshet. Modelling cell polarization driven by synthetic spatially graded rac activation. *PLoS computational biology*, 8(6):e1002366, 2012.
- [20] Pablo A Iglesias and Peter N Devreotes. Navigating through models of chemotaxis. *Current opinion in cell biology*, 20(1):35–40, 2008.
- [21] Pablo A Iglesias and Peter N Devreotes. Biased excitable networks: how cells direct motion in response to gradients. *Current opinion in cell biology*, 24(2):245–253, 2012.
- [22] Aron B Jaffe and Alan Hall. Rho gtpases: biochemistry and biology. *Annu. Rev. Cell Dev. Biol.*, 21:247–269, 2005.
- [23] Alexandra Jilkine and Leah Edelstein-Keshet. A comparison of mathematical models for polarization of single eukaryotic cells in response to guided cues. *PLoS computational biology*, 7(4):e1001121, 2011.

- [24] Alexandra Jilkine, Athanasius FM Marée, and Leah Edelstein-Keshet. Mathematical model for spatial segregation of the rho-family gtpases based on inhibitory crosstalk. *Bulletin of mathematical biology*, 69(6):1943–1978, 2007.
- [25] Robert R Kay, Paul Langridge, David Traynor, and Oliver Hoeller. Changing directions in the study of chemotaxis. *Nature Reviews Molecular Cell Biology*, 9(6):455–463, 2008.
- [26] Michael M Kozlov and Alex Mogilner. Model of polarization and bistability of cell fragments. *Biophysical journal*, 93(11):3811–3819, 2007.
- [27] Andre Levchenko and Pablo A Iglesias. Models of eukaryotic gradient sensing: application to chemotaxis of amoebae and neutrophils. *Biophysical journal*, 82(1):50–63, 2002.
- [28] Benjamin Lin, William R Holmes, C Joanne Wang, Tasuku Ueno, Andrew Harwell, Leah Edelstein-Keshet, Takanari Inoue, and Andre Levchenko. Synthetic spatially graded rac activation drives cell polarization and movement. *Proceedings of the National Academy of Sciences*, 109(52):E3668–E3677, 2012.
- [29] Chun-Min Lo, Hong-Bei Wang, Micah Dembo, and Yu-li Wang. Cell movement is guided by the rigidity of the substrate. *Biophysical journal*, 79(1):144–152, 2000.
- [30] Joseph A Madri and Donnasue Graesser. Cell migration in the immune system: the evolving inter-related roles of adhesion molecules and proteinases. *Journal of Immunology Research*, 7(2-4):103–116, 2000.
- [31] Athanasius FM Marée, Verônica A Grieneisen, and Leah Edelstein-Keshet. How cells integrate complex stimuli: the effect of feedback from phosphoinositides and cell shape on cell polarization and motility. *PLoS Comput Biol*, 8(3):e1002402–e1002402, 2012.
- [32] Athanasius FM Marée, Alexandra Jilkine, Adriana Dawes, Verônica A Grieneisen, and Leah Edelstein-Keshet. Polarization and movement of keratocytes: a multiscale modelling approach. *Bulletin of mathematical biology*, 68(5):1169–1211, 2006.
- [33] Stuart McLaughlin and Alan Aderem. The myristoyl-electrostatic switch: a modulator of reversible protein-membrane interactions. *Trends in biochemical sciences*, 20(7):272–276, 1995.
- [34] Hans Meinhardt. Orientation of chemotactic cells and growth cones: models and mechanisms. *Journal of Cell Science*, 112(17):2867–2874, 1999.
- [35] Hans Meinhardt and A Gierer. Applications of a theory of biological pattern formation based on lateral inhibition. *Journal of cell science*, 15(2):321–346, 1974.
- [36] Hans Meinhardt and Alfred Gierer. Pattern formation by local self-activation and lateral inhibition. *Bioessays*, 22(8):753–760, 2000.

- [37] Jason Meyers, Jennifer Craig, and David J Odde. Potential for control of signaling pathways via cell size and shape. *Current biology*, 16(17):1685–1693, 2006.
- [38] Alex Mogilner and Kinneret Keren. The shape of motile cells. *Current Biology*, 19(17):R762–R771, 2009.
- [39] Alex Mogilner and George Oster. Force generation by actin polymerization ii: the elastic ratchet and tethered filaments. *Biophysical journal*, 84(3):1591–1605, 2003.
- [40] Konstadinos Moissoglou, Boris M Slepchenko, Nahum Meller, Alan F Horwitz, and Martin A Schwartz. In vivo dynamics of rac-membrane interactions. *Molecular biology of the cell*, 17(6):2770–2779, 2006.
- [41] Arun Murali and Krishnaraj Rajalingam. Small rho gtpases in the control of cell shape and mobility. *Cellular and Molecular Life Sciences*, 71(9):1703–1721, 2014.
- [42] Mikiya Otsuji, Shuji Ishihara, Kozo Kaibuchi, Atsushi Mochizuki, Shinya Kuroda, et al. A mass conserved reaction–diffusion system captures properties of cell polarity. *PLoS computational biology*, 3(6):e108, 2007.
- [43] Ryan J Petrie, Andrew D Doyle, and Kenneth M Yamada. Random versus directionally persistent cell migration. *Nature Reviews Molecular Cell Biology*, 10(8):538–549, 2009.
- [44] Thomas D Pollard. Regulation of actin filament assembly by arp2/3 complex and formins. *Annu. Rev. Biophys. Biomol. Struct.*, 36:451–477, 2007.
- [45] Myrto Raftopoulou and Alan Hall. Cell migration: Rho gtpases lead the way. *Developmental biology*, 265(1):23–32, 2004.
- [46] Anne J Ridley, Martin A Schwartz, Keith Burridge, Richard A Firtel, Mark H Ginsberg, Gary Borisy, J Thomas Parsons, and Alan Rick Horwitz. Cell migration: integrating signals from front to back. *Science*, 302(5651):1704–1709, 2003.
- [47] Gillian L Ryan, Heather M Petroccia, Naoki Watanabe, and Dimitrios Vavylonis. Excitable actin dynamics in lamellipodial protrusion and retraction. *Biophysical journal*, 102(7):1493–1502, 2012.
- [48] Guy Servant, Orion D Weiner, Paul Herzmark, Tamás Balla, John W Sedat, and Henry R Bourne. Polarization of chemoattractant receptor signaling during neutrophil chemotaxis. *Science*, 287(5455):1037–1040, 2000.
- [49] Alan Mathison Turing. The chemical basis of morphogenesis. *Philosophical Transactions of the Royal Society of London B: Biological Sciences*, 237(641):37–72, 1952.
- [50] Peter JM Van Haastert and Peter N Devreotes. Chemotaxis: signalling the way forward. *Nature reviews Molecular cell biology*, 5(8):626–634, 2004.

- [51] Ben Vanderlei, James J Feng, and Leah Edelstein-Keshet. A computational model of cell polarization and motility coupling mechanics and biochemistry. *Multiscale Modeling & Simulation*, 9(4):1420–1443, 2011.
- [52] George H Wadhams and Judith P Armitage. Making sense of it all: bacterial chemotaxis. *Nature Reviews Molecular Cell Biology*, 5(12):1024–1037, 2004.
- [53] Neng Yang, Osamu Higuchi, Kazumasa Ohashi, Kyoko Nagata, Atsushi Wada, Kenji Kangawa, Eisuke Nishida, and Kensaku Mizuno. Cofilin phosphorylation by lim-kinase 1 and its role in rac-mediated actin reorganization. *Nature*, 393(6687):809–812, 1998.
- [54] Muhammad H Zaman, Linda M Trapani, Alisha L Sieminski, Drew MacKellar, Haiyan Gong, Roger D Kamm, Alan Wells, Douglas A Lauffenburger, and Paul Matsudaira. Migration of tumor cells in 3d matrices is governed by matrix stiffness along with cell-matrix adhesion and proteolysis. *Proceedings of the National Academy of Sciences*, 103(29):10889–10894, 2006.
- [55] A Zemel, F Rehfeldt, AEX Brown, DE Discher, and SA Safran. Cell shape, spreading symmetry, and the polarization of stress-fibers in cells. *Journal of Physics: Condensed Matter*, 22(19):194110, 2010.

A Derivation of a Model for Membrane-Cytosol Binding

In this section, we derive the basic equations for the membrane-cytosol binding/unbinding model, which we used to model molecules such as the small GTPases, which can exist both in a membrane bound state, as well as sequestered in the cytosol.

A.1 3D Membrane-Cytosol Interaction Model

As in the main part of the paper, we denote by c the density of molecules which are freely diffusing in the cytosol, measured in moles per volume, and by m the density of membrane-bound molecules, measures in moles per area. L_I is the interaction length such that when a molecule in the cytosol is within a distance less or equal to L_I of the membrane, there is a probability of binding this molecule to the membrane. The associated binding rate is denoted by \tilde{k}_{on} . Likewise, unbinding is denoted k_{off} , and the diffusion coefficients for diffusion in the cytosol or on the membrane, respectively, are denoted D_C and D_M . Then, m and c evolve according to the following PDEs:

$$\begin{aligned}\frac{\partial m(\bar{r}_m, t)}{\partial t} &= D_M \nabla_2^2 m(\bar{r}_m, t) + \tilde{k}_{on} \int_{|\bar{r}_m - \bar{r}_c| \leq L_I} c(\bar{r}_c, t) - k_{off} m(\bar{r}_m, t) \\ \frac{\partial c(\bar{r}_c, t)}{\partial t} &= D_C \nabla_3^2 c(\bar{r}_c, t)\end{aligned}\tag{9}$$

If Ω denotes the domain, i.e. the inside of the cell, then $\bar{r}_c \in \Omega$ denotes a point inside of the cell. Likewise, $\partial\Omega$ denotes the boundary of the cell, i.e. the membrane, so $\bar{r}_m \in \partial\Omega$ denotes a point on the membrane. Naturally, the first is defined on $\partial\Omega$, and the second equation is defined on Ω . Furthermore, we have assumed that all molecules which are with a distance of L_I to a point on the membrane \bar{r}_m are equally likely to be bound with a rate of \tilde{k}_{on} , which could be generalized by including a kernel in the integral such that molecules closer to the membrane are more likely to bind. However, we assume that L_I is small (see the discussion in the appendix section A.3.2) so that c does not significantly vary on this length scale, and the membrane is not significantly curved on this scale. Hence, all molecules in the cytosol within a half-sphere with radius L_I contribute to binding to the membrane (and influence the membrane-bound densities of a disk with radius L_I around the point \bar{r}_m under consideration). Hence, we can simplify $\tilde{k}_{on} \int_{|\bar{r}_m - \bar{r}_c| \leq L_I} c(\bar{r}_c, t) = k_{on} L_I c(\bar{r}_m, t)$, where k_{on} only differs from \tilde{k}_{on} by a numerical factor. We hence get the following resulting equations:

$$\begin{aligned}\frac{\partial m(\bar{r}_m, t)}{\partial t} &= D_M \nabla_2^2 m(\bar{r}_m, t) + k_{on} L_I c(\bar{r}_m, t) - k_{off} m(\bar{r}_m, t) \\ \frac{\partial c(\bar{r}_c, t)}{\partial t} &= D_C \nabla_3^2 c(\bar{r}_c, t) \\ -D_C e_n \nabla c(\bar{r}_m, t) &= k_{on} L_I c(\bar{r}_m, t) - k_{off} m(\bar{r}_m, t).\end{aligned}\tag{10}$$

Here, we have included the boundary condition for c which ensures conservation of the number of molecules under binding and unbinding, and e_n is the unit normal vector at the membrane. These are identical to equation (1) in the main part of the paper, which we have used for all subsequent results.

A.2 Alternative Derivation from a Discrete Model

We now give an alternative derivation of equation (1) from a discrete model. We consider a small section of a cell near the cell membrane, so small that we can ignore the curvature of the membrane. Such section is shown in a schematic drawing on the right panel of Fig. 6, where the cell membrane is highlighted by the red surface. We are interested in the dynamics of the binding and unbinding of molecules to the membrane. Let L_I be the interaction length such that when a molecule in the cytosol is within a distance less or equal to L_I of the membrane, there is a probability of binding this molecule to the membrane. The associated binding rate is denoted by k_{on} . Likewise, unbinding is denoted k_{off} .

We define the domain of interest to be a cube of length $L \gg L_I$, which we discretize into equally spaced small cubes of size δ . Initially, we identify $\delta = L_I$. Each cube is labeled by integer-valued indices (k, l, m) , and the membrane is located at the boundary $m = 0$. Then $M(k, l)$ denotes the number of membrane-bound molecules at the membrane segment adjacent to cube $(k, l, 0)$, and $C(k, l, m)$ denotes the number of cytosolic molecules in the cube (k, l, m) . We consider the following processes: In the inner part of the cytosol, unbound molecules can diffuse only. At the cube adjacent to the membrane, they can diffuse in parallel to the membrane or away from the membrane, or they can bind to the membrane. On the other hand, membrane-bound molecules can unbind, or diffuse on the membrane. The following equations describe the rate of changes of the average number of molecules:

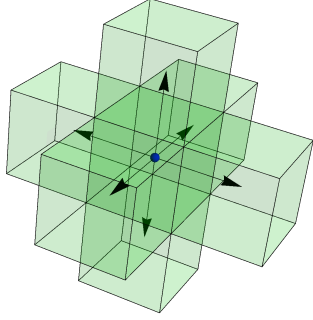
$$\begin{aligned} \frac{\partial M(k, l)}{\partial t} &= \frac{D_M}{\delta^2} (M(k+1, l) + M(k-1, l) + M(k, l+1) + M(k, l-1) - 4M(k, l)) + \\ &\quad k_{on}C(k, l, 0) - k_{off}M(k, l), \\ \frac{\partial C(k, l, m)}{\partial t} &= \frac{D_C}{\delta^2} (C(k+1, l, m) + C(k-1, l, m) + C(k, l+1, m) + C(k, l-1, m) \\ &\quad + C(k, l, m+1) + C(k, l, m-1) - 6C(k, l, m)), \quad m > 0, \\ \frac{\partial C(k, l, 0)}{\partial t} &= \frac{D_C}{\delta^2} (C(k+1, l, 0) + C(k-1, l, 0) + C(k, l+1, 0) + C(k, l-1, 0) \\ &\quad + C(k, l, 1) - 5C(k, l, 0)) + k_{off}M(k, l) - k_{on}C(k, l, 0). \end{aligned} \quad (11)$$

We now want to study the continuum limit of those equations. First, we add an artificial layer of cubes at $m = -1$, such that

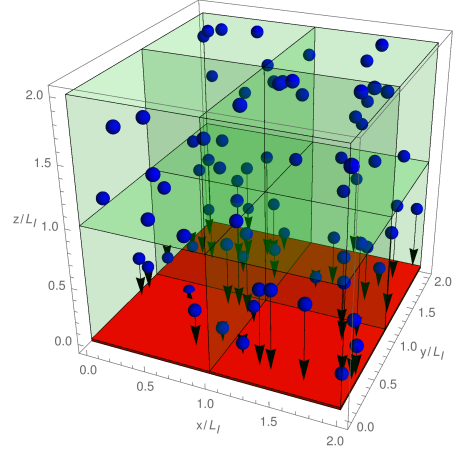
$$C(k, l, -1) := \frac{\delta^2}{D_c} (k_{off}M(k, l) - k_{on}C(k, l, 0)) + C(k, l, 0). \quad (12)$$

The advantage is that we can now combine the last two equations of (11) into

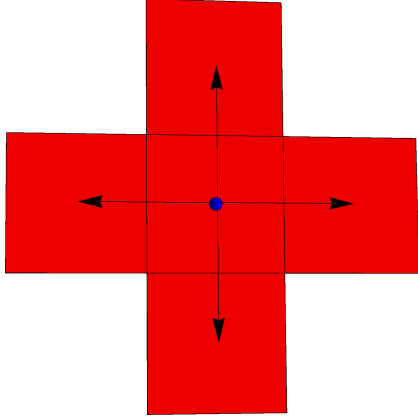
$$\begin{aligned} \frac{\partial C(k, l, m)}{\partial t} &= \frac{D_C}{\delta^2} (C(k+1, l, m) + C(k-1, l, m) + C(k, l+1, m) + C(k, l-1, m) \\ &\quad + C(k, l, m+1) + C(k, l, m-1) - 6C(k, l, m)), \quad m > -1, \end{aligned} \quad (13)$$



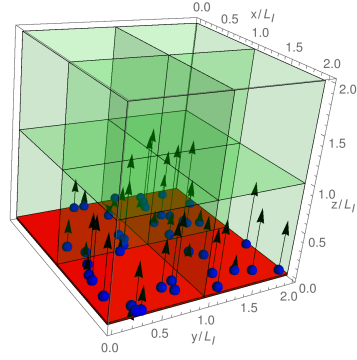
(a) Diffusion in cytosol



(b) Binding to the membrane



(c) Diffusion on membrane



(d) Unbinding from the membrane

Figure 6: Molecules in the cytosol can move from their current cube to any of the nearest-neighbor cubes (Figure (a)), or, if they are within a distance of the interaction range L_I to the membrane, they can bind to the membrane (Figure (b)). Membrane-bound molecules can diffuse on the membrane only (Figure(c)), or unbind from the membrane (Figure (d)).

which is supplemented by (12). From those equations, it is straight-forward to take the continuum limit $\delta \rightarrow 0$. We define $c(x, y, z) = \frac{C(k, l, m)}{\delta^3}$ to be the density of unbound molecules at a point (x, y, z) , where we identify $(x, y, z) = (\delta k, \delta l, \delta m)$, and likewise $m(x, y) = \frac{M(k, l)}{\delta^2}$ is the surface density of molecules bound to the membrane. Then, the continuum limit $\delta \rightarrow 0$ gives the following equation:

$$\begin{aligned} \frac{\partial m(x, y)}{\partial t} &= D_M \nabla_2^2 m(x, y) + k_{on} \int_0^{L_I} c(x, y, z) dz - k_{off} m(x, y) \\ \frac{\partial c(x, y, z)}{\partial t} &= D_C \nabla_3^2 c(x, y) \\ D_C \frac{\partial c(x, y, 0)}{\partial z} &= k_{on} \int_0^{L_I} c(x, y, z) dz - k_{off} m(x, y). \end{aligned} \quad (14)$$

We have introduced the two and three-dimensional Laplace operators, ∇_2^2 and ∇_3^2 , respectively. If we assume that the concentration in the cytosol does not vary much on a length scale of L_I , we can reduce these equations to the local model given by equation (1).

A.3 One-Dimensional Reduction

We consider a cylindrical cell where the height of the cell is L and the radius is R , such that $L \gg R$. We choose cylindrical coordinates (r, ϕ, z) such that $r \in [0, R]$, $z \in [0, L]$ and cylindrical symmetry, so our fields m and c do not depend on $\phi \in [0, 2\pi]$. As m is the concentration of membrane bound protein, it is only defined at the boundary of the cell located at $r = R$ and $z = 0, L$. Furthermore, we assume that the dependence of c on r is weak, relative to the dependence on z , and completely neglect the r dependence of m as this would only matter at $x = 0, L$.

The PDEs in cylindrical coordinates then become

$$\begin{aligned} \frac{\partial m(z, t)}{\partial t} &= D_M \partial_z^2 m(z, t) + k_{on} L_I c(R, z, t) - k_{off} m(z, t) \\ \frac{\partial c(r, z, t)}{\partial t} &= D_C \left(\partial_z^2 + \frac{1}{r} \partial_r r \partial_r \right) c(r, z, t) \\ D_C \partial_r c(R, z, t) &= -k_{on} L_I c(R, z, t) + k_{off} m(z, t), \\ D_C \partial_z c(r, 0, t) &= k_{on} L_I c(r, 0, t) - k_{off} m(0, t), \\ D_C \partial_z c(r, L, t) &= -k_{on} L_I c(r, L, t) + k_{off} m(L, t). \end{aligned} \quad (15)$$

Then, let us define the following one-dimensional densities

$$\begin{aligned} \tilde{c}(z, t) &= \int_0^R \int_0^{2\pi} c(r, z, t) r d\phi dr \\ &= 2\pi \int_0^R c(r, z, t) r dr, \\ \tilde{m}(z, t) &= \int_0^{2\pi} m(z, t) R d\phi = 2\pi R m(z, t). \end{aligned} \quad (16)$$

As R is assumed to be small such that diffusion in the radial direction is faster than other timescales in the problem, we assume that the unbound densities depend only weakly on r and expand $\tilde{c}(z, t)$ to get

$$\begin{aligned}\tilde{c}(z, t) &= 2\pi \int_0^R (c(R, z, t) + \partial_r c(R, z, t)(r - R) + \dots) r dr \\ &\approx 2\pi \left(c(R, z, t) \frac{R^2}{2} - \frac{R^3}{6} \frac{1}{D_C} (k_{off} m(z, t) - k_{on} L_I c(R, z, t)) \right) \\ &= \pi R^2 \left(1 + \frac{R L_I}{3 D_C} k_{on} \right) c(R, z, t) - \frac{k_{off} R^2}{6 D_C} \tilde{m}(z, t).\end{aligned}\quad (17)$$

Here, we have expanded about $r = R$ and used the boundary condition. If we further assume that the radius R and the interaction range L_I are small such that the dimensionless number

$$\frac{R L_I k_{on}}{3 D_C} \ll 1, \quad \frac{k_{off} R^2}{6 D_C} \ll 1, \quad (18)$$

then we can approximate further (see appendix section A.3.2 for a discussion of those parameters)

$$\tilde{c}(z, t) \approx \pi R^2 c(R, z, t). \quad (19)$$

The one-dimensional densities follow the differential equations

$$\begin{aligned}\frac{\partial \tilde{m}(z, t)}{\partial t} &= D_M \partial_z^2 \tilde{m}(z, t) + 2\pi R k_{on} L_I c(R, z, t) - k_{off} \tilde{m}(z, t), \\ &= D_M \partial_z^2 \tilde{m}(z, t) + 2k_{on} \frac{L_I}{R} \tilde{c}(z, t) - k_{off} \tilde{m}(z, t), \\ \frac{\partial \tilde{c}(z, t)}{\partial t} &= D_C \left(\partial_z^2 \tilde{c}(z, t) + \int_0^R \left(\frac{1}{r} \partial_r r \partial_r c(r, z, t) \right) 2\pi r dr \right), \\ &= D_C \left(\partial_z^2 \tilde{c}(z, t) + 2\pi R \partial_r c(R, z, t) \right), \\ &= D_C \left(\partial_z^2 \tilde{c}(z, t) + 2\pi R \frac{1}{D_C} (k_{off} m(z, t) - k_{on} L_I c(z, t)) \right), \\ &= D_C \partial_z^2 \tilde{c}(z, t) + \left(k_{off} \tilde{m}(z, t) - 2k_{on} \frac{L_I}{R} \tilde{c}(z, t) \right),\end{aligned}\quad (20)$$

which were given in the main text in equation (2). Mass conservation is ensured by accompanying those equations by Neumann No-flux boundary conditions. Note that while these equations are perfectly one-dimensional PDEs, with the spatial domain defined by the length of the cylinder, the cylinder radius is still felt in the sense that the membrane-binding rate k_{on} is effectively renormalized by the inverse of the cylinder radius R .

A.3.1 One-dimensional Reduction on a general geometry

We now briefly outline the derivation of a one-dimensional model when the geometry is not symmetric. If we reduce the model along the z -axis, we consider

$A(z)$ and $\Gamma(z)$ to be the z -dependent measures such that the reduced densities $\tilde{c}(z, t) = A(z)c(x, y, z, t)$, $\tilde{m}(z, t) = \Gamma(z)m(x, y, z, t)$ are one-dimensional densities in the sense that $\tilde{c}(z, t)dz$ and $\tilde{m}(z, t)dz$ denote the number of molecules in a length segment of length dz around position z . For z -independent geometries such as a cylinder, or rectangular shapes, $A(z)$ and $\Gamma(z)$ are simply the cross-sectional area and the circumference, respectively. It is then straight-forward to show that these reduced, one-dimensional densities follow the following equations:

$$\begin{aligned}\frac{\partial \tilde{m}(z, t)}{\partial t} &= \partial_z \left(D_M \Gamma(z) \partial_z \frac{\tilde{m}(z, t)}{\Gamma(z)} \right) + k_{on} L_I \frac{\Gamma(z)}{A(z)} \tilde{c}(z, t) - k_{off} \tilde{m}(z, t), \\ \frac{\partial \tilde{c}(z, t)}{\partial t} &= \partial_z \left(D_C A(z) \partial_z \frac{\tilde{c}(z, t)}{A(z)} \right) - k_{on} L_I \frac{\Gamma(z)}{A(z)} \tilde{c}(z, t) + k_{off} \tilde{m}(z, t).\end{aligned}\quad (21)$$

A.3.2 GTPase Parameter Estimation

We now investigate when the use of the one-dimensional model is justified for the case where the molecule is a small GTPase. We have $D_C = 100 \mu m^2/s$ [7, 28]. Furthermore, we estimate that the interaction range of the binding reaction, L_I , approximately corresponds to the size of the molecules. We have a molecular weight of the small GTPases of about $21 kDa$. Exact size determination of proteins is tricky [10], but here we only need a rough estimate, which gives that we have a volume of $V = \frac{21 * 1.6 * 10^{-27} kg}{1 kg/l} = 3 * 10^{-26} m^3 = 30 nm^3$. Hence, the interaction length scale is on the order of a few nanometers. We put $L_I = 2 nm$, and this estimate is similar to stimations made in similar contexts [33]. Furthermore, we can safely assume that $R \gg L_I$ for realistic cell geometries. Then, unless $k_{on} \gg k_{off}$, of the two requirements $\frac{R L_I k_{on}}{3 D_C} \ll 1$, $\frac{k_{off} R^2}{6 D_C} \ll 1$, the first one automatically holds provided the second one does. From [40] we can estimate that k_{off} should be faster than $k_{off} = 0.06 s^{-1}$, as the combined deactivation/unbinding rate² is of this magnitude. However, the actual binding and unbinding rates are influenced by the presence of other regulators such as GDI molecules [8] and might be different for GTP and GDP bound GTPases, and is hence also influenced by the presence of GEFs and GAPs. Here, we focus on rough estimates and use the above numbers to derive a limit for the radial length scale of

$$R \ll \sqrt{\frac{6 D_C}{k_{off}}} \leq \sqrt{\frac{600}{0.06}} \mu m = 100 \mu m. \quad (22)$$

As long as k_{off} is not too large this condition is satisfied for realistic cell dimensions. However, if k_{off} should be significantly larger than estimated above then this limit might be hard to satisfy.

Now we look at the steady-state assumption between bound and unbound GTPase. For this, we have

$$L \gg \sqrt{\frac{D_C}{k_{off}}}. \quad (23)$$

²This combined rate is denoted k_{off} in [40].

With $k_{off} = 0.06s^{-1}$, we get $L \gg 30\mu m$ would safely satisfy this constraint. However, most likely k_{off} is significantly larger so the steady-state assumption is most likely valid for shorter cells as well.

A.4 Two-Dimensional Reduction

Let us consider a flat cell, which, for simplicity, we take to be a disk of radius R and height h . Hence, it is natural to choose cylindrical coordinates, and the full model is described by (15), with L replaced by h . We now consider the limit $h \ll R$. Then, we can rewrite the z -dependence of the Laplacian as

$$\begin{aligned} D_C \frac{\partial^2 c(r, \phi, z, t)}{\partial z^2} &\approx D_C \frac{\partial_z c(r, \phi, h) - \partial_z c(r, \phi, 0)}{h}, \\ &= \frac{k_{off}}{h} (m(r, h, t) + m(r, 0, t)) - \frac{k_{on} L_I}{h} (c(r, \phi, h, t) + c(r, \phi, 0, t)). \end{aligned} \quad (24)$$

If the concentrations only depend very weakly on z , then we can simplify the system by introducing

$$\begin{aligned} \tilde{c}(r, \phi, t) &= \int_0^h c(r, \phi, z, t) dz = hc(r, \phi, t), \\ \tilde{m}(r, \phi, t) &= 2m(r, \phi, t), \end{aligned} \quad (25)$$

and get

$$\begin{aligned} \frac{\partial \tilde{m}(r, \phi, t)}{\partial t} &= D_M \nabla_2^2 \tilde{m}(r, \phi, t) + 2k_{on} \frac{L_I}{h} \tilde{c}(r, \phi, t) - k_{off} \tilde{m}(r, \phi, t), \\ \frac{\partial \tilde{c}(r, \phi, t)}{\partial t} &= D_C \nabla_2^2 \tilde{c}(r, \phi, t) - 2k_{on} \frac{L_I}{h} \tilde{c}(r, \phi, t) + k_{off} \tilde{m}(r, \phi, t), \end{aligned} \quad (26)$$

which coincide with equations (7). Introducing $\tilde{k}_{on} = 2k_{on} \frac{L_I}{h}$ we formally recover the two-dimensional model used in [32]. Similarly to the one-dimensional case, the scaling of the parameters is different. As before, we consider the steady-state solution where f denotes the fraction of membrane-bound molecules. Hence, for the flat cylinder we get

$$f = \frac{k_{on}}{k_{on} + k_{off} \frac{h}{2L_I}}. \quad (27)$$

B 3D Polarization Pathway

In this section, we discuss the three-dimensional version of a cell polarization pathway introduced in a one-dimensional model of a cell in [19].

B.1 Model Setup

The one-dimensional model of [19] was motivated by experiments where cells were constrained in effective one-dimensional geometries. It was assumed that

the approximate three-dimensional geometry is rectangular with length scales $L \gg w > d$, with an initial length of $L = 20\mu m$. The volume of a cell in the experimental paper [28], which uses the model of [19], was given as approximately $V = 800\mu m^3$. The supplementary information of [28] mentions $d = 0.2\mu m$, which seems a bit small for a real cell and would also imply that $w = 200\mu m$ at the given volume. We hence compare to a cell with base measure $L, w, d = 20, 8, 5\mu m$. In [28], the cells were about $80\mu m$ long (see e.g. Figure S4 in [28]), which would, at the same volume, be compatible with $L, w, d = 80, 5, 2\mu m$. Such cell seems also compatible with the one-dimensional limit as described in section 2.2 of the main text. In [19, 28] the change in cell length was taken into account by changing the fraction of membrane bound to unbound inactive molecules via equation (4), which is, however, slightly different to our result. The three-dimensional model will automatically take into account any geometry change. The basic equations for the evolution of the three GTPases now takes into account that the each GTPase can exist in an active, membrane bound form m_a , a membrane bound, inactive form m_i and a form c which diffuses inactively through the cytosol. These follow the principal scheme

$$\begin{aligned}\frac{\partial m_a}{\partial t} &= D_M \Delta m_a + I_G m_i - \delta_G m_a, \\ \frac{\partial m_i}{\partial t} &= D_M \Delta m_i - I_G m_i + \delta_G m_a + k_{on} L_I c|_{\partial\Omega} - k_{off} m_i, \\ \frac{\partial c}{\partial t} &= D_C \Delta c, \\ -D_C e_n \nabla c|_{\partial\Omega} &= k_{on} L_I c|_{\partial\Omega} - k_{off} m_i.\end{aligned}\tag{28}$$

Here, I_G represents the activation, and δ_G the deactivation rate, whereas k_{on}, k_{off} denote the binding and unbinding rates as in section 2. Note that equations (28) are slightly different from the equations given in the appendix of [19], which were used to motivate the one-dimensional model from a three-dimensional perspective.

We note that to account for the proper localization of the membrane bound and unbound species m_a, m_i and c , we measure c in Molar, but m_a, m_i in $\frac{mol}{m^2}$. Whereas this latter measure is not often chosen in experiments, as usually total cell concentrations are measured, this is nevertheless the physically more meaningful measure, as m_a, m_i denote number molecules per two dimensional membrane area, and this choice ensures that our equations and the dimensional reductions have the correct units. To compare with [19], we will hence multiply the concentrations of active GTPases with $\frac{V_0}{S_0} = \frac{800\mu m^3}{600\mu m^2} = 4/3\mu m$, the fraction of volume to surface area for the above mentioned rectangular cell of basic length $L, w, d = 20, 8, 5\mu m$.

The full model involving the three GTPases Rho, Rac and Cdc42 as well as PIP, PIP2 and PIP3, which are all assumed to be purely membrane bound, is given

by the following equations:

$$\begin{aligned}
\frac{\partial[\text{Rac}_a]}{\partial t} &= D_M \nabla^2[\text{Rac}_a] - \delta_R[\text{Rac}_a] + I_R \frac{[\text{Rac}_{mi}]}{\text{Rac}_{tot,2}} \\
\frac{\partial[\text{Rac}_{mi}]}{\partial t} &= D_M \nabla^2[\text{Rac}_{mi}] + \delta_R[\text{Rac}_a] - I_R \frac{[\text{Rac}_{mi}]}{\text{Rac}_{tot,2}} + k_{on} L_I \text{Rac}_{ci}|_{\partial\Omega} - k_{off} \text{Rac}_{mi} \\
\frac{\partial[\text{Rac}_{ci}]}{\partial t} &= D_C \nabla^2[\text{Rac}_{ci}] \\
-D_C e_n \nabla \text{Rac}_{ci}|_{\partial\Omega} &= k_{on} L_I \text{Rac}_{ci}|_{\partial\Omega} - k_{off} \text{Rac}_{mi} \\
\frac{\partial[\text{Rho}_a]}{\partial t} &= D_M \nabla^2[\text{Rho}_a] - \delta_\rho[\text{Rho}_a] + I_{\text{Rho}} \frac{[\text{Rho}_{mi}]}{\text{Rho}_{tot,2}} \\
\frac{\partial[\text{Rho}_{mi}]}{\partial t} &= D_M \nabla^2[\text{Rho}_{mi}] + \delta_\rho[\text{Rho}_a] - I_{\text{Rho}} \frac{[\text{Rho}_{mi}]}{\text{Rho}_{tot,2}} + k_{on} L_I \text{Rho}_{ci}|_{\partial\Omega} - k_{off} \text{Rho}_{mi} \\
\frac{\partial[\text{Rho}_{ci}]}{\partial t} &= D_C \nabla^2[\text{Rho}_{ci}] \\
-D_C e_n \nabla \text{Rho}_{ci}|_{\partial\Omega} &= k_{on} L_I \text{Rho}_{ci}|_{\partial\Omega} - k_{off} \text{Rho}_{mi} \\
\frac{\partial[\text{Cdc42}_a]}{\partial t} &= D_M \nabla^2[\text{Cdc42}_a] - \delta_C[\text{Cdc42}_a] + I_{\text{Cdc}} \frac{[\text{Cdc42}_{mi}]}{\text{Cdc}_{tot,2}} \\
\frac{\partial[\text{Cdc42}_{mi}]}{\partial t} &= D_M \nabla^2[\text{Cdc42}_{mi}] + \delta_C[\text{Cdc42}_a] - I_{\text{Cdc}} \frac{[\text{Cdc42}_{mi}]}{\text{Cdc}_{tot,2}} + k_{on} L_I \text{Cdc42}_{ci}|_{\partial\Omega} - k_{off} \text{Cdc42}_{mi} \\
\frac{\partial[\text{Cdc42}_{mi}]}{\partial t} &= D_C \nabla^2[\text{Cdc42}_{mi}] \\
-D_C e_n \nabla \text{Cdc42}_{ci}|_{\partial\Omega} &= k_{on} L_I \text{Cdc42}_{ci}|_{\partial\Omega} - k_{off} \text{Cdc42}_{mi} \\
\frac{\partial[\text{PIP}]}{\partial t} &= D_P \nabla^2[\text{PIP}] - \delta_{P_1}[\text{PIP}] + I_{P_1} + k_{21}[\text{PIP}_2] - \frac{k_{\text{PI5K}}}{2} \left(1 + \frac{[\text{Rac}_a]}{\text{Rac}_{tot,2}} \right) [\text{PIP}] \\
\frac{\partial[\text{PIP}_2]}{\partial t} &= D_P \nabla^2[\text{PIP}_2] - k_{21}[\text{PIP}_2] + \frac{k_{\text{PI5K}}}{2} \left(1 + \frac{[\text{Rac}_a]}{\text{Rac}_{tot,2}} \right) [\text{PIP}] \\
&\quad - \frac{k_{\text{PI3K}}}{2} \left(1 + \frac{[\text{Rac}_a]}{\text{Rac}_{tot,2}} \right) [\text{PIP}_2] + \frac{k_{\text{PTEN}}}{2} \left(1 + \frac{[\text{Rho}_a]}{\text{Rho}_{tot,2}} \right) [\text{PIP}_3] \\
\frac{\partial[\text{PIP}_3]}{\partial t} &= D_P \nabla^2[\text{PIP}_3] + \frac{k_{\text{PI3K}}}{2} \left(1 + \frac{[\text{Rac}_a]}{\text{Rac}_{tot,2}} \right) [\text{PIP}_2] - \frac{k_{\text{PTEN}}}{2} \left(1 + \frac{[\text{Rho}_a]}{\text{Rho}_{tot,2}} \right) [\text{PIP}_3]
\end{aligned} \tag{29}$$

Here, the activation functions I_G are given by

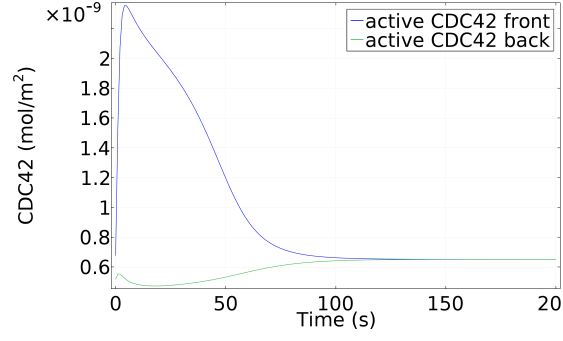
$$\begin{aligned}
I_R &= \left(I_{R1} + I_{R2} f_1 \frac{[\text{PIP}_3]}{P_{3b}} + \alpha[\text{Cdc42}_a] + S(\mathbf{x}, t) \right), \\
I_{\text{Rho}} &= \frac{I_{\text{Rho}}}{1 + \left(\frac{[\text{Rac}_a]}{a_2} \right)^n}, \\
I_{\text{Cdc}} &= \frac{I_{\text{Cdc}}}{1 + \left(\frac{[\text{Rho}_a]}{a_1} \right)^n}.
\end{aligned} \tag{30}$$

The stimulus gradient $S(\mathbf{x}, t)$ can be applied in the direction of an external growth factor stimulus. All coefficients apart from the membrane binding and

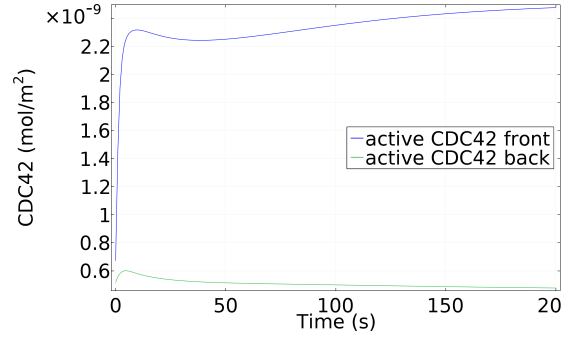
unbinding rates are taken from [19, 28], but those which multiply a membrane density are multiplied by the factor $\frac{V_0}{S_0}$. Furthermore, to compare the activation rates given in [19, 28] with ours we need to divide them with the fraction of bound to total inactive molecules f , as we separately consider bound and unbound inactive GTPases. All parameters are summarized in Table 1. Lacking accurate measurements of k_{off} , it is commonly believed that k_{off} is much faster larger than the deactivation rate [40, 19]. As the deactivation rates were estimated in [19] to be $1s^{-1}$, we take $k_{off} = 10s^{-1}$. While the total unbinding/deactivation rate was estimated in [40] to be much smaller than $1s^{-1}$, we stick to those values here as we first would like to compare our three-dimensional model to the one-dimensional model of [19]. In subsection 3.2 in the main text we study the influence of varying k_{off} on the polarization behavior of the cell. We also need to determine the combination of parameters $k_{on}L_I$. From the estimates of D_C, D_M , combined with the estimate that at baseline length of $L = 20\mu m$ the diffusion coefficient for total inactive GTPases (bound and unbound) is $50\mu m^2/s$, we get that about half of the inactive GTPases molecules are typically membrane bound. This equilibrium value can then be used to deduce $k_{on}L_I$ via equation (5).

Dimensional parameter	Estimate
D_C	$100 \mu\text{m}^2 \text{s}^{-1}$
D_M	$1 \mu\text{m}^2 \text{s}^{-1}$
D_P	$5 \mu\text{m}^2 \text{s}^{-1}$
$\text{Rac}_{tot,2}$	10nmol m^{-2}
$\text{Rho}_{tot,2}$	4nmol m^{-2}
$\text{Cdc}_{tot,2}$	3.4nmol m^{-2}
P_{3b}	0.2nmol m^{-2}
δ_R	1s^{-1}
δ_ρ	1s^{-1}
δ_C	1s^{-1}
δ_{P_1}	0.21s^{-1}
k_{21}	0.021s^{-1}
k_{\max}	2.8s^{-1}
k_{P_2}	2.1s^{-1}
α	1.3s^{-1}
μ_P	0.011s^{-1}
G	0.03s^{-1}
I_{R1}	$0.4 \mu\text{M s}^{-1}$
I_{R2}	$0.4 \mu\text{M s}^{-1}$
I_{Rho}	$13.2 \mu\text{Ms}^{-1}$
I_{Cdc}	$5.9 \mu\text{Ms}^{-1}$
I_{P_1}	$14 \text{nmol m}^{-2} \text{s}^{-1}$
a_1	1.7nmol m^{-2}
a_2	1.3nmol m^{-2}
k_{PI5K}	0.084s^{-1}
k_{PI3K}	0.00072s^{-1}
k_{PTEN}	0.432s^{-1}
f_1	1
k_{off}	10s^{-1}
$k_{\text{on}} L_I$	$13.3 \mu\text{m s}^{-1}$

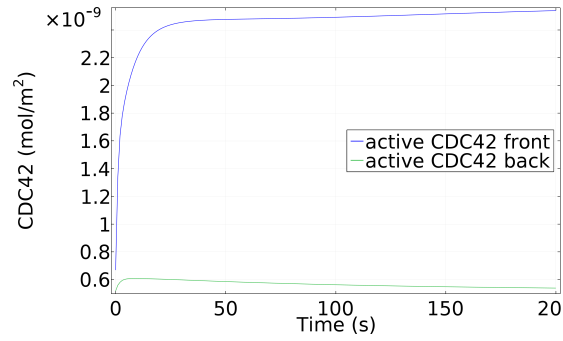
Table 1: Parameters of the cell polarization model equation (29), inferred for a cell with dimensions $L, w, d = 20, 8, 5 \mu\text{m}$, so all values which multiply membrane concentrations are rescaled by the factor $\frac{V_0}{S_0} = \frac{4}{3} \mu\text{m}$. This means $1 \mu\text{M} \frac{V_0}{S_0} = \frac{4}{3} \frac{\text{nmol}}{\text{m}^2}$. Furthermore, α , I_{R1} , I_{R2} , I_{Rho} and I_{Cdc} are multiplied by the baseline fraction of bound inactive molecules f . We have also rounded the parameters as appropriate.



(a) $L=20\mu m$



(b) $L=40\mu m$



(c) $L=80\mu m$

Figure 7: The time evolution of concentration of active CDC42 in time at the front and back of the rectangular cells as shown in Figures 1 and 2.